PVA/nanocellulose nanocomposite membranes for CO_2 separation from flue gas

Jonathan Ø. Torstensen, Ragne M.L. Helberg, Liyuan Deng, Øyvind W. Gregersen, Kristin Syverud

The Norwegian University of Science and Technology, Høgskoleringen 1, 7491 Trondheim, Norway
RISE PFI, 7491 Trondheim, Norway

ABSTRACT

In this paper, we explore the use of nanocelluloses as an additive to poly (vinyl alcohol) (PVA) nanocomposite membranes for CO_2/N_2 mixed-gas separation. Our findings are that several types of nanocellulose can be used to improve membrane performance. PVA/cellulose nanocrystals (CNC) nanocomposite membranes have the most promising performance, with increased CO_2 permeance (127.8 ± 5.5 GPU) and increased CO_2/N_2 separation factor (39 ± 0.4) compared to PVA composite membranes, with permeance 105.5 ± 1.9 GPU and separation factor 36 ± 0.5. The performance of PVA/CNC membranes is similar compared to PVA/carbon nanotubes (CNTs) membranes shown earlier. Thus, CNTs can be replaced by CNC that is biodegradable and non-toxic. Investigating several different nanocellulose types reveal that a high nanocellulose charge and small nano-cellulose particles are important nanocellulose traits that improve membrane performance.

1. Introduction

CO$_2$ capture and storage (CCS) is a growing field, aiming at reducing the amount of CO_2 released into the atmosphere by industry (Stuart Haszeldine, 2009). Release of CO_2 into the atmosphere is a consequence of increasing industrialization and consumption of resources, and it is projected to increase in the future (Davis et al., 2010). The need for more efficient CO_2 capture is thus in high demand. The leading technology of industrial gaseous CO_2 – capture is liquid amine absorption (Cuéllar-Franca and Azapagic, 2015), but it is also possible to capture CO_2 by absorption onto solids (Cuéllar-Franca and Azapagic, 2015) or by the use of membranes (Brunetti et al., 2010; Cuéllar-Franca and Azapagic, 2015). Amine absorbers/strippers are large, their operation is expensive and careful operator attention is required. In addition, it is highly energy consuming and solvent regeneration over time is needed (Favre, 2007). Using membranes can be advantageous over amine absorption as this technique possibly requires the same amount of energy, less space and can be produced with materials and methods that are more friendly to the environment (Favre, 2007). The key property of gas separation membranes is their ability to control the rate of permeation of different gases in a mixture. The selective separation of gases is a result of difference in size, shape and physiochemical properties of the molecules in the feed stream (Mulder, 1996). Most of the current commercial gas separation membranes are based on dense polymeric materials, which separate gas mixtures by the solution-diffusion mechanism (Baker and Low, 2014). Polymeric membranes have several advantages, including good processability, good mechanical properties and low cost (Mahajan et al., 2002). However, most polymeric membranes are subjected to a trade-off between permeability and selectivity; polymers that are highly permeable are usually low-selective and vice versa. The Robeson upper bound is a physical threshold describing this trade-off relationship (Robeson, 2008, 1991) and solutions to overcome it are presented by Brunetti et al. (Brunetti et al., 2010) A promising approach is so-called facilitated transport (Deng, 2009; Deng et al., 2009; Kim et al., 2004; Saeed and Deng, 2015). As an example, the amino groups in the PVAm/PVA membrane of Deng (Deng, 2009) catalyze the conversion of CO_2 to $HCO_3{}^-/CO_3{}^{2-}$ in the membrane. These ions have higher diffusion constants than CO_2 and transport is thus faster (Deng and Hägg, 2010). Finally, CO_2 is regained at the sweep side. One approach has been to use polymeric membranes

(poly (vinyl alcohol)) embedded with a carbonic anhydrase synthetic analogue (Saeed and Deng, 2015). This membrane showed a separation factor (CO_2/N_2) of 107 and CO_2 permeance in the range of 255.5 GPU at high relative humidities ($\sim$ 95%) (Saeed and Deng, 2015). This membrane has been reinforced by carbon nanotubes (CNTs) to improve performance, with a CO_2/N_2 ideal selectivity of 120 and CO_2 permeance of 362.9 GPU (Saeed and Deng, 2016). Previous studies show that the addition of CNTs improves swelling capacity and enhances mechanical strength which improved the CO_2 separation performance of the membrane (Saeed and Deng, 2016).

Nanocellulose has previously been used for biomedical (Rashad et al., 2017) and packaging (Ottesen et al., 2017) applications and as a nanocomposite additive to enhance material, chemical and thermal properties, (Li et al., 2014) and to fabricate smart materials (Auad et al., 2008). In this paper we explore the use of nanocelluloses as a nanofiller in a poly (vinyl alcohol) membrane designed to separate flue-gas (mixed gas, CO_2/N_2) at low pressures ($\Delta P = 0.2$ bar). The underlying motivation has been to investigate if the addition of nanocellulose itself may improve the performance, and possibly replace carbon nanotubes in the future. This has been done previously for CNC, with natural gas (Ansaloni et al., 2017b; Jahan et al., 2018) and flue gas (Ansaloni et al., 2017b). In this study several other nanocelluloses were tested and membrane behavior was explained by investigating properties of the different nanocelluloses and PVA/nanocellulose nanocomposites. Nanocelluloses are biodegradable, non-toxic, and to some extent commercially available. We have compared commercially available **c**ellulose **n**ano**c**rystals (CNC) with in-house produced TEMPO-oxidized and phosphorylated **c**ellulose **n**ano**f**ibrils (CNF). We chose CNC as it is commercially available and because the crystals are small ($\sim$ nm in width and length direction) and are relatively uniform in size and shape. TEMPO-oxidized CNF (TO-CNF) was chosen as it gives the opportunity to vary the nanocellulose charge, and to a certain extent the nanocellulose dimensions. Phosphorylated CNF was chosen as it can be produced to have higher charge than both TO-CNF and CNC. The membranes were fabricated as 4 wt% PVA/nanocellulose nanocomposites. One concentration was chosen as this is a screening study. This is a concentration where nanocellulose does not have a too large impact on the suspension viscosity. While nanocellulose nancomposites have been previously tested as CO_2 separation membranes, the purpose of this paper is to discern good predictors of choosing the appropriate nanocellulose both in terms of suspension and nanocomposite film properties, as well as obtaining a hypothesis on how nanocellulose affects transport properties. To our knowledge this has not yet been realized.

2. Experimental

2.1. Materials

2.1.1. Poly (vinyl alcohol)

Poly (vinyl alcohol), PVA, was purchased from Sigma-Aldrich, 87–89% hydrolyzed, M_w 85000–124,000 (CAS no. 9002-89-5). It was dissolved in deionized water giving $\sim$ 3 wt.% stock solution. PVA was added while stirring and the solution was placed at 90 °C for 3 h, before stirring overnight. The solution was then filtered using a 5 μm syringe filter. The stock solution was used no later than six weeks from preparation, and kept refrigerated.

2.1.2. Polysulfone support

The polysulfone (Psf) support was acquired from Alfa Laval (Lund, Sweden), with a 50 000 Da molecular weight cut-off (MWCO). The support thickness was $\sim$ 130 μm thick, with a dense top skin layer. The polysulfone support porosity was asymmetric with increasing porosity from the top-layer.

2.1.3. Cellulose pulp

Fully bleached cellulose pulp from softwood was supplied by Södra for the preparation of TEMPO-oxidized nanocellulose and phosphorylated nanocellulose. Chemical characterization has previously been done on the as-received cellulose pulp (Torstensen et al., 2018).

2.1.4. TEMPO oxidized nanocellulose

The cellulose pulp was oxidized at ambient temperatures using 99% TEMPO ((2,2,6,6-tetramethylpiperidin-1-yl)oxyl) (Sigma-Aldrich, Missouri, USA), sodium bromide (NaBr; > 99%, Sigma-Aldrich, Missouri, USA) and sodium hypochlorite (NaClO, Roth, Germany). The oxidation follows the procedure as devised by Saito et al. (Saito and Isogai, 2004). A solution of 0.0125 g/g pulp TEMPO and 0.125 g/g pulp NaBr was prepared in deionized water the day of oxidation. The solution was added to a given amount of pulp that had been stirred for 10 min. The suspension was diluted to 1.33 vol % and stirred for 5 min. Oxidation was done by adding different amounts of NaClO at a rate of 0.013 mol once every 60 s. For the low charge type (L-CNF) the total amount of NaClO was 2 mmol/g, while it was 5 mmol/g for the high charge type (H-CNF). The amount of dry mass that was oxidized was $\sim$ 120 g in both cases. During the oxidation, pH was maintained at 10.5 by gradually adding 0.5 M NaOH (Fisher Scientific, New Hampshire, USA). When pH remained constant over a period of 10 min, the reaction was said to be completed and the suspension was neutralized to pH 7 using 0.5 M HCl (Fisher Scientific, New Hampshire, USA). The oxidized pulp was filtered with deionized water until the effluent had a conductivity < 5 μS/cm, and stored at 4 °C until fibrillation. The TEMPO-oxidized pulp was diluted to 0.8 wt% prior to fibrillation.

2.1.5. Phosphorylated nanocellulose

Phosphorylated nanocellulose (P-CNF) was fabricated using a protocol based on the work of Ghanadpour et al. (Ghanadpour et al., 2015) 150 g of pulp was mixed with a solution of urea (ACS reagent, Sigma Aldrich, Missouri, USA) and ammonium phosphate dibasic (99%, Sigma Aldrich, Missouri, USA), in a molar relationship of AGU: $(NH_4)_2HPO_4$:urea – 1:2.5:10. It was assumed that all pulp was anhydrous glucose units (AGU). The suspension was diluted to 1.33 wt% and stirred for 6 h in ambient conditions. It was dried completely at 60 °C ($\sim$ 14 days). The mass was subjected to 150 °C for 50 min. It was dissolved in deionized water and filtered with deionized water until the conductivity of the effluent was < 10 μs/cm, and stored at 4 °C until fibrillation. The phosphorylated pulp was diluted to 0.8 wt% and beaten (10,000 rounds) with a L&W Pulp Disintegrator to get an even suspension prior to fibrillation.

2.1.6. Fibrillation

Fibrillation is a mechanical treatment were chemically treated cellulose pulp is subjected to a large shear force to obtain nanocellulose. The TEMPO oxidized and phosphorylated nanocellulose was fibrillated by homogenization. Homogenization was done using a Rannie 15 type 12.56X homogenizer (APV, SPX Flow Technology, Silkeborg, Denmark), with one pass at 600 bar, followed by one pass at 1000 bar.

2.1.7. Cellulose nanocrystals

Cellulose nanocrystals, CNC was purchased from The University of Maine, Forest Products Laboratory (sulfuric acid process (Postek et al., 2013), slurry, $\sim$ 12 wt%).

2.2. Composite membrane and self-supported film preparation

PVA stock solution (pH $\sim$ 5) was mixed with nanocellulose to a 2 g/100 g suspension, with 1.92 g PVA and 0.08 g nanocellulose, yielding a final film/membrane of 96 wt% PVA and 4 wt% nanocellulose. The pure PVA membranewas prepared as a 2 g/100 g solution. The exact dry matter of both PVA solutions and nanocelluloses was measured prior to solution/suspension preparation. Suspension/solutions were

stirred over night at 800 RPM with a magnetic stirrer. Suspensions were then sonicated for 10 min at 60% efficiency using a probe sonicator (130 W, Sonics Vibra-Cell™). The pure PVA solution was not sonicated. Suspensions/solutions were either cast as membranes or self-supported films.

2.2.1. Composite membranes

In this paper a composite membrane means that the membrane is a laminar composite with an active membrane layer coated on a polysulfone support membrane. The term nanocomposite membrane is used to clarify that the active layer itself is a matrix/nanofiller type composite (PVA and nanocellulose), which in turn is part of a composite membrane. PVA or nanocomposite membranes were prepared by dip coating the flat polysulfone support membrane with either PVA solution or a PVA/nanocellulose suspension. Prior to dip coating, the support was loosely attached with aluminum tape to a glass plate and washed in tap water (45–55 °C) for 1.5 h followed by washing with DI water for 5 min. The support was then sealed with aluminum tape to make sure that no coating suspension/solution would penetrate the backside of the membrane. The support was manually immersed in the coating suspension/solution for 30 s. After 3 h standing vertically, the once coated Psf support was turned 180° before it was again immersed in the coating suspension/solution for 30 s. The membrane was kept drying at ambient conditions for approximately 12 h, standing vertically. Keeping the membrane vertical during drying ensures that excess suspension/solution runs off the membrane. Initial drying was followed by drying at 45 °C in a convective oven for 3 h to ensure a smooth evaporation of water. Finally, the membrane was heat-treated at 105 °C for 1 h before further testing.

2.2.2. Self supported PVA- and nanocomposite film preparation

The prepared nanocomposite suspensions were cast with 50 mL in a circular PE petri-dish (diameter: 95 mm, height: 15 mm) and films were dried at 35 °C. Films were then heated as for membranes. Initial drying was followed by drying at 45 °C in a convective oven for 3 h to ensure a smooth evaporation of water. Finally, the film was heat-treated at 105 °C for 1 h before further testing.

2.3. Experimental setup and measurements

2.3.1. Membrane testing and characterization

2.3.1.1. Humid mixed gas permeation test. Membrane gas separation performance under humid conditions was measured using a constant pressure-variable volume method in a mixed gas separation system as shown in Fig. 1. All gases were supplied by AGA (Oslo, Norway) and details about the set-up is described elsewhere (Saeed and Deng, 2015). The steady-state flux of two components in a mixed gas stream permeating through a membrane is measured in this test. A mixed gas of 10% CO_2 and 90% N_2 was used as a feed gas and CH_4 was used as a sweep gas. The purpose of a sweep gas is to ensure correct GC pressure. The relative humidity of both the feed gas and the sweep gas was adjusted to 95% for all experiments by two sets of mass flow controllers. The use of a humid sweep gas was done in order to retain the proper humidity during experiments.

All experiments were carried out at a temperature of 23 °C, a feed pressure of 1.2 bars and a sweep pressure of 1 bar. The feed flow rate was set to 200 mL/min and the sweep flow rate 100 mL/min by Bronkhorst flow meters for all experiments. The process parameters (pressure, temperature, gas flow rate and relative humidity of gases of feed and sweep streams) were continuously monitored and logged by LabView Software (National Instruments, Texas, USA). The total pressure was regulated by a back-pressure regulator. The permeate and the retentate flow rates were measured by a bubble flow meter. The feed and sweep gas stream concentrations were analyzed continuously by a Micro GC Agilent 3000. The membrane was placed in a circular stainless steel permeation cell, with an active permeation area of 19.7 cm².

For the membrane separation setup, the stage-cut was calculated to be 0.77%.

In this study the mixed gas CO_2 permeance and N_2 permeance was calculated using a complete mixing model from the total permeance flow as described by Eq. (1) (Mulder, 1996). Permeance was calculated as the average of minimum 2 h measurement after steady-state is reached.

$$P = J/(y_f p_f - y_p p_p) \ [GPU] \tag{1}$$

P represents the permeance [GPU], J is the flux, y_f and y_P are the mole fraction of gas at feed and permeate side respectively. The absolute pressures in bar are p_f and p_p, on the feed side and permeate side respectively (f denotes feed side, p denotes permeate side).

In this study, the thickness weighed permeability (Pe_T, Eq. (2)) was calculated using the measured permeance values (P) and membrane thickness (t) obtained by SEM:

$$Pe_T = P \times t \ [GPU \times cm]. \tag{2}$$

Membrane CO_2/N_2 separation factor (α_{CO_2/N_2}) in a CO_2/N_2 gas stream is defined by Eq. (3), and determines the degree of gas-separation (Mulder, 1996). It was calculated from the mole-fractions (y) on the feed-side (f) and permeate (p) side:

$$\alpha_{CO_2/N_2} = \frac{\frac{y_{CO_2}^p}{y_{N_2}^p}}{\frac{y_{CO_2}^f}{y_{N_2}^f}}. \tag{3}$$

2.3.1.2. Scanning electron microscopy (SEM). Membranes were imaged using a Hitachi TM3030 SEM. The membranes were freeze-fractured with liquid N_2 in order to get an even cross section. The membranes were placed on a sample holder using carbon tape before coating it with a thin layer of gold. The gold coating was applied in an Argon atmosphere with a Quorum Q150 ES sputter coater (20 mA for 60 s, ~15 nm). The SEM pictures were taken with back-scattered electron mode at 15 kV voltage. Membrane thicknesses were measured after membrane permeation testing. For each membrane type, one membrane sample was used and more than 2 cross-sections were investigated from a minimum of two different sample locations. The minimal investigated membrane length was 15 μm. The thickness was measured using ImageJ with a custom made PlugIn (Chinga et al., 2007). The active layer was manually removed from the support membrane in ImageJ. Images were then thresholded in ImageJ using auto-threshold (Images- > Adjust- > Threshold- > Auto-threshold). The built in plugin measures the height of each active layer pixel-column. The thickness is the average of all measurements (n) which were collected from a total number of samples from different membrane locations (N).

2.3.2. Nanocellulose characterization

2.3.2.1. Fibertester. Fibertester measurements were done with 2×0.1 g of nanocellulose dry matter, on a Lorentzen and Wettre FiberTester PLUS. Reported values are average values. The fibertester gives several characteristics of the nanocellulose pulp. Fines are defined as particles with a length < 200 μm (ISO standard). Objects are defined as having length between 100 μm and 10 000 μm and width between 75 μm and 10 000 μm. Reported errors are average value deviation from min/max values.

2.3.2.2. Nanocellulose morphology, dimensions and geometrical percolation. Width. Atomic Force Microscopy (AFM) samples were prepared by depositing diluted nanocellulose suspensions (0.001 wt%) on a Mika-surface, and drying them with an N_2 gun. AFM was performed in tapping mode. The nanofibril and nanocrystal width was extracted from height measurements in AFM images. The height
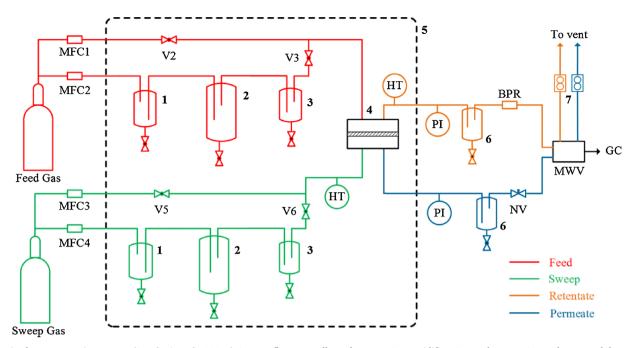
Fig. 1. Mixed gas permeation set up. (Ansaloni et al., 2017a) 1: Mass flow controller-safety trap; 2: Humidifier; 3: Droplet trap; 4: Membrane module; 5: Heated cabinet; 6: Water knockout; 7: Bubble flowmeters; MFC: mass flow controller; NV: Needle valve; BPR: Back pressure regulator; PI: Pressure indicator; HT: Humidity and temperature sensor; MWV: Multi-way valve; GC: Gas chromatograph.

was used because measuring the actual width gives artefacts in the form of a convolution between the AFM-tip and the nanofibril/crystal (Sacui et al., 2014). The image used measured $3\,\mu m \times 3\,\mu m$ (1024 pixels $\times$ 1024 pixels). AFM images were processed in Gwyddion. Images were preprocessed by aligning rows according to the median of differences and level data by mean plane subtraction. The height was measured on $N > 15$ nanocelluloses, with five measurements per CNF and three per CNC. One measurement constituted a line-profile across the fibril/crystal width, and the line was five pixels wide. The nanocellulose maximum height (V_{MAX}) was taken as the maximum profile height using the extract profile tool. Even after image preprocessing, the background showed some unevenness. Thus, the baseline (V_{MIN}) was defined as the average of the lowest intensity value on each side of the fibril/crystal. The nanocellulose width was defined as in Eq. (4). Reported errors are standard deviations

$$W_{AFM} = V_{MAX} - V_{MIN}.$$ (4)

Length. The nanocellulose length was measured by dynamic light scattering (DLS) using a Malvern Zetasizer ZS S3600. Both 0.01 wt% and 0.001 wt% suspensions were prepared by light stirring and measured at ambient conditions. For each sample, 10 runs of 15 measurements of 30 s were done. Measurements were intensity average. Reported errors are standard deviations. Methods from Gamelas et al. (Gamelas et al., 2015) were used to correlate DLS length with actual fibril length. This was done as DLS measures the hydrodynamic diameter and not the actual fibril (CNF) length. For CNC, the length was measured manually from AFM images.

The geometrical percolation threshold (Favier et al., 1997) (GT, Eq. (5)) is the concentration at which composite fillers physically touch each other in the polymer matrix, thus forming a continuous network throughout the material.

$$GT = 100\,\% \times \frac{0.7}{\frac{L}{d}} \times r \ [wt\%]$$ (5)

The percolation threshold calculation assumes monodisperse nanocellulose with a certain length, L, and width d, and $r = \rho_{nanocellulose}/$

ρ_{pva}. The nanocomposite contains 96 wt% PVA ($\rho = 1.22\,g/cm^3$, given by supplier) and 4 wt% nanocellulose ($\rho = 1.57\,g/cm^3$ for CNC, otherwise $\rho = 1.55\,g/cm^3$, (Science et al., 1970)). Cellulose nanocrystals (CNC) are made from 60% 1α (Sacui et al., 2014), with a density (Sugiyama et al., 1991) of $1.58\,g/cm^3$. The CNC density is thus calculated to be $0.6 \times 1.58 + 0.4 \times 1.55 = 1.57\,g/cm^3$.

2.3.2.3. Nanocellulose charge. The P-CNF, L-CNF and H-CNF charge was determined after fibrillation. The charge of CNF type nanocelluloses was measured by minimum two parallels with a conductiometric method (Saito and Isogai, 2004). The sulfur content in CNC and phosphorous content in P-CNF was measured using elemental absorption, ICP-MS, two parallels. Reported errors are average value deviation from min/max values.

2.3.3. Nanocomposites characterization
2.3.3.1. Swelling. Swelling tests were done gravimetrically in a Termaks Environmental Chamber, by subjecting self-supported films to water vapour at 90 ($\pm$ 0.4) %RH at 23.4 ($\pm$ 0.3) ℃. All swelling experiments were done with three replicate films, each with a starting dry weight of 0.8–1 g. Films were kept in a desiccator until swelling tests were performed (at least 16 h). Weighings were done by transferring the film to a four decimal analytical scale.

Film swelling (S) was characterized by the weight of the film prior to swelling (W_0) and the weight after a given time (W_t) in the humidity chamber. Swelling was calculated (Eq. (6)) after 144 h, which was found sufficient to reach swelling equilibrium

$$S = \left(\left(\frac{W_t}{W_0}\right) - 1\right) \times 100\,\%.$$ (6)

For each weighing, the average value of three replicates was used to describe swelling. The standard error (SE) was calculated from the standard deviation (σ), with n = 3 (the number of replicates), and used to describe experimental error

$$SE = \frac{\sigma}{\sqrt{n}}.$$ (7)

2.3.3.2. DSC. Differential scanning calorimetry (DSC) was done using a NETSCH Polyma 214. The sample was heated from 10 °C to 120 °C once, with 10 °C/min heating rate, and 10 min plateau at 10 °C and 120 °C. It was then cooled (10 °C/min) to 10 °C, with a 10 min plateau. The second cycle was 10 °C – 350 °C, with a heating rate of 10 °C/min. The enthalpy of melting, ΔH_M, was estimated from the second cycle. This was used to estimate the film crystal mass fraction (Dufresne, 2012) (X_C, Eq. (8)) and the filler weight fraction, φ, was 0 for pure PVA films, otherwise 0.04. DSC was done on dry samples that had been stored in a desiccator prior to analysis

$$X_C = \frac{\Delta H_M}{(1 - \varphi)\Delta H_M^0}. \tag{8}$$

The enthalpy of melting, ΔH_M^0, is the theoretical melting enthalpy of PVA 138.6 J/g (Peppas and Merrill, 1976). Reported errors are standard errors (Eq. (7)). As nanocelluloses do not melt, the reported results from DSC are measurements of PVA crystallinity.

2.3.3.3. XRD. X-ray diffraction was done using a D8 Focus. Films were investigated under ambient conditions, and for each film type two pieces of ~1.5 cm in diameter was investigated. Scattering profiles are the average curve, while the crystal size (L) was calculated from each individual profile. This was done using the Scherrer-equation (Klug et al., 1974) (Eq. (9)) where θ is the peak angle and B is the full-width half maximum ($\Delta(2\theta)$ in rad) and with K = 0.9, λ = 1.54 Å,

$$L = \frac{K \times \lambda}{B cos(\theta)}. \tag{9}$$

XRD was done on dry samples that had been stored in a desiccator prior to analysis. Reported errors are standard errors (Eq. (7)).

3. Results

3.1. Composite membrane characterization

A typical composite membrane is a dense polymer film coated on a polysulfone porous support membrane (Fig. 2).

Cross-sections investigated using SEM revealed that the thickness of the active layer varied with the type of nanocellulose that was used in the membrane (Table 1). It increased significantly compared to PVA membranes for all the nanocellulose types except L-CNF. This is attributed to the increased viscosity of the dip coating suspension, as membrane thickness increases with increasing suspension viscosity (Mulder, 1996). An increase in viscosity of the nanocomposite suspensions compared to PVA solutions was visually observed. Membranes were tested with a mixed gas constituting 10% CO_2 and 90% N_2. The stability of poly (vinyl amine) membranes in real flue gas has been tested previously (Sandru et al., 2013). Membranes retained
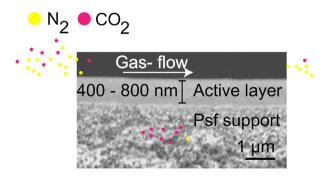

Fig. 2. Cross-section of a typical membrane, here exemplified by PVA/P-CNF. A dense PVA-film or PVA/nanocellulose nanocomposite active layer (top, grey, dense) is coated on an asymmetric porous polysulfone (Psf) support. The membrane/support interface is marked by a thin line. Scale-bar 1 μm. Cross-sections of other membranes are given in S1.

Table 1
Membrane thickness (t), membrane CO_2 permeance (Eq. (1)), thickness weighed permeability (Eq. (2)) and separation factor (Eq. (3)). N: number of different sample locations, n: total number of measurements.

Membrane	Thickness, t, (nm) ± SD (nm) (N, n)	P (CO_2) [GPU]	$Pe_T \times 10^3$ [GPU × cm]	CO_2/N_2 Separation factor/ideal selectivity
PVA	428 ± 57 (7, 6017)	105.5 ± 1.9	4.5 ± 0.6	36 ± 0.5 (42.5 ± 0.5[*])
PVA/L-CNF	491 ± 59 (5, 4652)	92.6 ± 3.7	4.5 ± 0.6	37.5 ± 0.5 (44 ± 4[*])
PVA/H-CNF	729 ± 42 (3, 2766)	90.7 ± 3.7	6.6 ± 0.5	42 ± 0.7 (50 ± 0[*])
PVA/P-CNF	770 ± 97 (4, 3699)	100 ± 3.7	7.7 ± 1	42 ± 1.8 (49 ± 0[*])
PVA/CNC	728 ± 136 (7, 6522)	127.8 ± 5.5	9.3 ± 1.8	39 ± 0.4 (48 ± 2[*])
PVA/1 wt% CNTs (Saeed and Deng, 2016)	830	125.9**	10.5**	50[*]

[*] Ideal selectivity P_{CO_2}/P_{N_2} where P is calculated from Eq. (1). ** Based on one thickness measurement of 830 nm in the referenced paper.

permeability and separation characteristics that were similar to lab-scale values over a period of 6 months. The flue gas contained high levels of SO_x, NO_x and some ash, and during the testing period, the factory had power shortage and technical difficulties. It is thus believed that the described membranes would be stable in realistic conditions. Membrane performance is given in Table 1. All membranes showed a slight increase in separation factor, with an increase from 36 (PVA) to 36–40 (nanocomposites). This is contrary to adding carbon nanotubes (CNTs) to PVA. In a study done by Saeed et al., (Saeed and Deng, 2016) membranes with 1% added CNTs had a 10% decrease in CO_2/N_2 ideal selectivity compared to neat PVA. In the current experimental work, increased CO_2/N_2 separation factor can be due to the increase in polar groups in the membrane (Kim et al., 2004), as the nanocellulose surfaces are charged as well as containing −OH-groups. Given the fact that the permeance is inversely proportional to the active layer thickness, (Mulder, 1996) the thickness weighed CO_2 permeability (Eq. (2)) is used rather than CO_2 permeance for comparison of the different membranes, as their thickness is not the same. PVA/CNC membranes had twice the thickness weighed CO_2-permeability with $(9.3 \pm 1.8) \times 10^{-3}$ GPU × cm, while neat PVA membranes had $(4.5 \pm 0.6) \times 10^{-3}$ GPU × cm. PVA/CNC membranes had a comparable performance compared to PVA with 1 wt% CNT (10.5×10^{-3} GPU × cm) (Saeed and Deng, 2016).

3.2. Nanocellulose characterization

The following section focuses on properties of the different nanocellulose types that make nanocellulose a suitable nanocomposite additive for membrane applications.

3.2.1. Fibertester

Fibertester was used to determine the amount of non nanoscopic structures (the partially degraded larger fibrils and partially digested plant cells) in the different nanocellulose suspensions (Table 2). Fines are present at the highest percentage in CNC and H-CNF, indicating that most of the fibers are < 200 μm. Moreover, objects are smaller compared to both L-CNF and P-CNF. The latter nanocelluloses are coarser in the sense that they contain i) less fines ii) more objects and iii) larger objects compared to CNC and H-CNF. P-CNF contains both larger objects and less fines compared to L-CNF. L-CNF had the most objects. This signifies that P-CNF has larger and less numerous population of

Table 2
Overview over nanocellulose properties.

	L-CNF	H-CNF	P-CNF	CNC
Dimensions of nanofraction				
Width(W_{AFM}) (nm) ([#])	2.05 ± 0.52 (18)	3.35 ± 0.77 (17)	2.85 ± 0.6 (20)	7 ± 1.6
Length (DLS) (nm)	1563 ± 268	699 ± 142	2163 ± 821	154 ± 45[**]
Geometrical percolation threshold (wt%)	0.1	0.4	0.1	4.1
Fibertester				
Fines (%)	78.7 ± 0.4	93.4 ± 3.1	50.2 ± 1.65	98.5 ± 1
Object count/g	76,903 ± 7350	9646[*]	37,504 ± 480	804[*]
Object length (μm)	208 ± 7	178[*]	317 ± 35	187[*]
Object width (μm)	122.5 ± 0.5	119[*]	151 ± 26	140[*]
Charge (μmol/g)				
Conductometric method	716 ± 20	1510 ± 54	1866 ± 12.5	–
Elemental absorption	–	–	1644.8 (822.4 ± 1.6 × 2)	317.4 ± 7.6
Charged group	-COO-	-COO-	O-HPO$_3^-$ /O-PO$_3^{2-}$	O-SO$_3$-
pKa	3.6 (Fujisawa et al., 2011)	3.6 (Fujisawa et al., 2011)	~1 and ~6 (McElroy and Glass, 1951; van Wazer, 1958)	2.8 (Ehmann et al., 2014)

[#] Number of nanocelluloses.

[*] Values are taken from the one replicate where objects were measured.

[**] Measured by AFM.

non-nano objects.

3.2.2. Nanocellulose morphology, dimensions and geometrical percolation

AFM of different nanocelluloses showed that all CNF types had the typical fibril shape (Sacui et al., 2014), while CNC was shorter, rod shaped crystals (Fig. 3). The nanocellulose width was found from AFM images (Eq. (4), width in Table 2) and length was determined by dynamic light scattering (DLS) on 0.001 wt% suspensions for CNF types (Length in Table 2) (complete DLS data included in S2), while AFM was used for CNC (Table 2). Widths obtained from AFM measurements were consistent with others (Rodionova et al., 2013), with ~ 3 nm for CNF types and ~ 7 nm for CNC. In the case of CNC, widths were comparable

to Sacui et al. (Sacui et al., 2014) which found the CNC (same supplier, same chemical process) width to be 5.9 nm ± 1.8 nm and length 130 nm ± 67 nm. We measured a width of 7 nm ± 1.6 nm (N = 16) nm and length from AFM images of CNC (N = 45), gave 151 nm ± 46 nm. Dynamic light scattering of 0.001 wt% CNC gave 159 nm ± 13 nm length.

Dynamic light scattering (DLS) of 0.001 wt% nanocellulose suspensions was done to find the cellulose nanofibril (-CNF) length. Based on the methods for length calculation from DLS reported by Gamelas et al., (Gamelas et al., 2015) length and width values from Table 2, were used to calculate the CNF lengths (S3). This was done as DLS does not measure the actual nanocellulose length, but the hydrodynamic
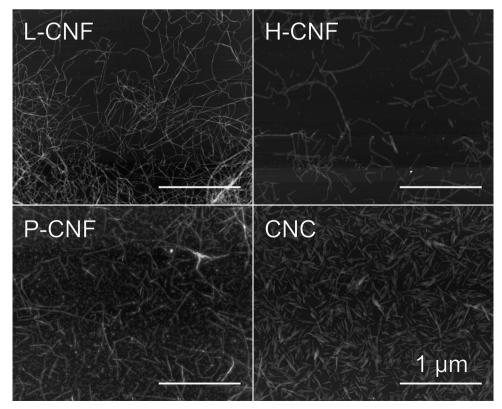

Fig. 3. AFM of the different nanocellulose types. Scale-bar 1 μm.

diameter. Based on the calculated values, it was reasoned that these approaches overestimated the nanocellulose length. This is probably due to the high aspect ratios of the CNF types used in this study (e. g. 233 for H-CNF and 759 for P-CNF). Moreover, the hydrodynamic diameter found directly from DLS is in good agreement with the fibril length reported by others (Ishii et al., 2011; Isogai et al., 2011; Sacui et al., 2014). It is thus reasoned that DLS hydrodynamic diameters directly represent an actual differences in length between the fibril types, and these length-values were used to calculate the geometrical percolation threshold. Geometrical percolation thresholds (Table 2, Eq. (5)) are below 0.5 wt% for all CNF types, and ∼4 wt% for CNC. In the case of CNC, using both literature values for dimensions (Sacui et al., 2014) as well as the length measured by DLS gives a geometrical percolation threshold < 4%. Moreover, it has been shown that if there is a distribution in nanocellulose length, the length needed to achieve the geometrical percolation decreases (Balberg and Binenbaum, 1983). For CNF types, Fibertester results indicate that the suspensions contain a significant non-nanoscale fraction. However, the calculated GT values are substantially lower than the added amounts. It is thus reasoned that all the nanocelluloses are geometrically percolated in the membrane and form a continuous network within the PVA matrix, provided that it is well dispersed in the matrix.

3.2.3. Nanocellulose charge

The nanocellulose charge was measured using a conductiometric method (Saito and Isogai, 2004) for TEMPO oxidized and phosphorylated CNF (P-CNF). CNC and P-CNF charge was measured using element absorption (for sulfur atoms in CNC, phosphorous atoms in P-CNF). In the case of CNC, charge values were consistent with claims from the manufacturer (∼0.01 g(sulfur)/g(CNC) sulfur content, corresponding to ∼313 μmol/g). Phosphorylated nanocellulose has two OH groups that can deprotonate (Ghanadpour et al., 2015), and charge measurements with a conductiometric method was compared to elemental absorption. Phosphorylated nanocellulose probed for phosphorous with elemental absorption, yielded phosphorous contents indicating a charge slightly lower than measured by conductiometry. The difference can be explained by the charge of the cellulose pulp (∼250 μmol/g) (Kumar et al., 2017). This charge is carboxylic acid groups and would not be measured by phosphorous atom absorption. The measured charge of phosphorylated CNF (Ghanadpour et al., 2015) and TEMPO oxidized CNF (Isogai et al., 2011) are in agreement with others.

3.3. Self supported PVA and nanocomposite film characterization

This section examines the properties of self-supported PVA and nanocomposite films. In order to understand how different nanocelluloses could change material properties to increase CO_2 permeance and/or CO_2/N_2 separation factor, self-supported PVA and nanocomposite films were examined with respect to swelling at 90 %RH and crystallinity by differential scanning calorimetry and XRD.

A high degree of swelling is believed to be important as it increases CO_2 to HCO_3^- conversion in membranes (Kim et al., 2004). Swelling was slightly reduced for all nanocomposites compared to neat PVA (Fig. 4). This reduction is small, and is most prominent in the PVA/P-CNF nanocomposite. Reduced swelling has been linked to strong filler/matrix interactions as well as strong hydrogen bonding between nanocelluloses (Svagan et al., 2009). Both of these factors are believed to contribute to decreased swelling in these nanocomposites. Both PVA and nanocellulose contain −OH groups on their surface, while hydrogen bonding between nanocellulose particles is considered to be abundant. Differential scanning calorimetry was done in order to measure the crystal mass fraction (X_C, Fig. 5). Melting peaks were obtained from the second cycle, after one cycle at 10 °C −120 °C. In the second cycle, melting peaks were found in the range 120 °C−200 °C. These were summed in order to obtain ΔH_M.

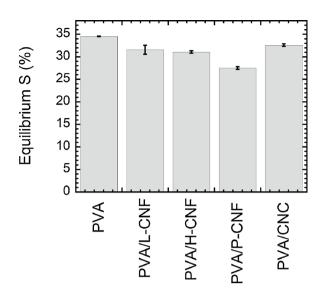The crystal mass fraction increased for all nanocomposites, from

Fig. 4. Composite equilibrium swelling (*S*, Eq. (6)). Complete values given in S4.
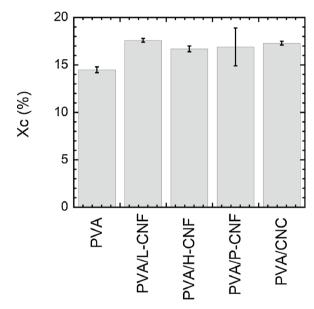

Fig. 5. PVA and nanocomposite crystal mass fraction (Eq. (8)). Complete values given in S4.

PVA at 14.5% to nanocomposites at 16.7–17.6 %. Neat PVA crystal mass fraction values are comparable to PVA found elsewhere (Liang et al., 2009). Based on literature, adding nanocellulose can both increase (Rescignano et al., 2014; Zhou et al., 2012), decrease (Abitbol et al., 2011; Alloin et al., 2011) and have no effect (Jalal Uddin et al., 2011) on the polymer matrix crystal mass fraction in nanocomposites. Slightly increased crystal mass fraction might also explain the slightly decreased swelling in Fig. 4, as water does not penetrate crystallites (Mihranyan et al., 2004).

XRD was done in order to more thoroughly examine the crystallinity of PVA and PVA/nanocellulose nanocomposites (Fig. 6). The major peak was located near 2θ = 19.4° and 20° corresponding well to the PVA [10Ī] and [101]-plane (Ricciardi et al., 2004). There was a slight right-shift asymmetry in nanocomposites which would be expected from adding nanocellulose, as it has a major peak at 2θ = 22.8° (Segal et al., 1959) (Table 3). Moreover, the crystal mean size was 2.8–3.1 nm, and there was no observable difference between composites and neat PVA, except that PVA/H-CNF composites had slightly larger crystals.
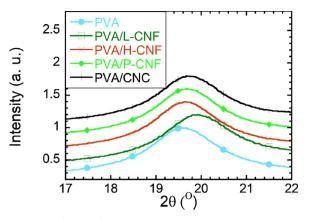
Fig. 6. XRD profiles of polymer and composite films. Diffraction peak values and crystal sizes and are given in Table 3.

Table 3
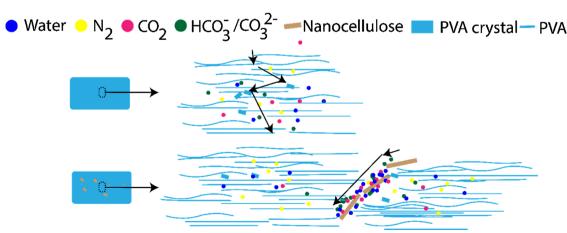XRD peak and crystallite size (*L*, Eq. (9)) of PVA and nanocomposites.

Type	Peak (2θ, °)	Mean crystallite size (nm)
PVA	19.63 ± 0.04	2.90 ± 0.05
PVA/L-CNF	19.88 ± 0.08	2.80 ± 0.01
PVA/H-CNF	19.68 ± 0.08	3.10 ± 0.01
PVA/P-CNF	19.69 ± 0.02	2.90 ± 0
PVA/CNC	19.74 ± 0.07	2.90 ± 0.05

Another interpretation of the extracted ʟ-values from the Debye-Scherrer equation, is that it represents the polymer chain spacing, (Zornoza et al., 2011) which indicates that the addition of nanocellulose does not compress or expand the PVA matrix, as observed for other nanofillers in PVA (Sharma et al., 2015a, 2015b, Sharma et al., 2014).

4. Discussion

In this paper we have tested the effect of four different nanocellulose types as fillers in PVA nanocomposites for CO_2/N_2 separation. All the nanocelluloses type improve the membrane performance, except gently TEMPO oxidized CNF (L-CNF). The best result was obtained using cellulose nanocrystals (CNC), which is the smallest and most monodisperse nanocellulose tested. We thus hypothesize that a small size is important because the small nanocellulose disperse better in the PVA matrix. In terms of nanocomposites, swelling is slightly reduced and crystal mass fraction slightly increased compared to PVA films. We believe that this affects membrane performance negatively. However,

these negative effects are similar in all nanocomposites. There is no evidence that nanocomposites change the N_2 permeance compared to PVA membranes (values in **S5**). Gently TEMPO oxidized CNF (L-CNF) is comparable in size to P-CNF, only the latter improves membrane function. This nanocellulose has a much higher charge compared to L-CNF and CNC. It is thus believed that a high charge is positive in terms of membrane performance, and can mitigate the negative effects of larger cellulose nanoparticles as well as more plant cell remnants present in the nanocellulose suspension. Further evidence of the importance of high charge/monodisperse nanocellulose is found as PVA/H-CNF nanocomposites also show an improvement compared to PVA membranes. The fact that high charge seems important raises the question of how nanocellulose improves the membrane CO_2 permeance. As all nanocelluloses are present above their geometrical percolation threshold, it is believed that the nanocellulose create a favorable path of diffusion through the active layer. Two factors influence the quality of such a path, namely dispersability and nanocellulose charge. The dispersion of nanocellulose is important to form a continuous network across the polymer matrix. In this sense, CNC is believed to have improved dispersability compared to P-CNF and H-CNF, mainly due to their smaller size. However, as P-CNF and H-CNF are more highly charged than CNC, this may improve their dispersability, still being less than that of CNC. The nanocellulose hydrophilicity and charge compared to PVA (neutral) is also believed to cause a redistribution of water from the entire nanocomposite to the PVA/nanocellulose interphase. Even though the water contents is lower in nanocomposites, compared to PVA films, we believe water is unevenly distributed with a higher concentration at the nanocellulose surface. This effect has been demonstrated for polymer/nanocellulose composites in other cases where there is a discrepancy between polymer/filler hydrophilicity (Dagnon et al., 2012). Water dense areas dissolve more CO_2 as this specie is more polar compared to N_2. A more highly charged nanocellulose surface will also by itself attract more CO_2 (Yu et al., 2013). If it is assumed that CNC has the best dispersability, this may explain why P-CNF and H-CNF still improve the membrane performance. They attract more water and CO_2 to the PVA/nanocellulose interface. Considering pKa values (Table 2) and that system pH is ~ 5 it is reasonable to believe that all the nanocellulose charged groups are close to fully ionized. In that case, P-CNF has the highest charge and thus attracts more water and CO_2. CO_2 will thus more readily be led in a pathway that guides the CO_2 molecule through the membrane in a geometrical percolated network, which is believed to be less tortuous than penetrating a pure PVA membrane by random pathways that can be impeded by e. g. PVA crystals. In addition to CO_2 being transported as CO_2 dissolved in water, it will also be transported as bicarbonate/carbonate (HCO_3^-/CO_3^{2-}), as this conversion is spontaneous. These ions will also be guided by the

Fig. 7. The addition of nanocellulose to PVA redistributes water and $CO_2/HCO_3^-/CO_3^{2-}$ in the nanocomposite to the nanocellulose/PVA interphase. This creates a favorable pathway for transport, where molecules can pass more easily due to higher gas/ion solubility and a less tortuous path.

same path, and it is reasonable to believe that CO_2 conversion to ions is slightly higher in more water-dense areas. The proposed transport mode and mechanisms are illustrated in Fig. 7. Other possible beneficial effects of employing nanocellulose is the possible increase in membrane stability over time.

5. Conclusion

In this paper we have evaluated cellulose nanocrystals (CNC), TEMPO oxidized cellulose nanofibrils and phosphorylated cellulose nanofibrils as nanofillers in poly (vinyl alcohol) composite membranes. We have found that PVA/CNC nanocomposites have the highest CO_2/N_2 separation factor (39) and CO_2 permeance (127.8 GPU) compared to neat PVA membranes with a separation factor of 36 and permeance of 105.5 GPU. PVA/CNC nanocomposite membranes are comparable to PVA/CNT membranes (carbon nanotubes) shown earlier, however CNCs are non-toxic and biodegradable. Phosphorylated and highly TEMPO oxidized nanofibrils also improve the performance, however, not as significant as CNC. Important predictors for a well suited nanocellulose quality are found to be a uniform, nanoscopic size distribution, with a high surface charge.

Acknowledgement

Appendix A. Supplementary data

Supplementary material related to this article can be found, in the online version, at doi:https://doi.org/10.1016/j.ijggc.2018.10.007.

References

Abitbol, T., Johnstone, T., Quinn, T.M., Gray, D.G., 2011. Reinforcement with cellulose nanocrystals of poly(vinyl alcohol) hydrogels prepared by cyclic freezing and thawing. Soft Matter 7, 2373. https://doi.org/10.1039/c0sm01172j.

Alloin, F., D'Aprea, A., Dufresne, A., Kissi, N.E., Bossard, F., 2011. Poly(oxyethylene) and ramie whiskers based nanocomposites: influence of processing: extrusion and casting/evaporation. Cellulose 18, 957–973. https://doi.org/10.1007/s10570-011-9543-x.

Ansaloni, L., Rennemo, R., Knuutila, H.K., Deng, L., 2017a. Development of membrane contactors using volatile amine-based absorbents for CO_2 capture: amine permeation through the membrane. J. Memb. Sci. 537, 272–282. https://doi.org/10.1016/j.memsci.2017.05.016.

Ansaloni, L., Salas-Gay, A., Ligi, S., Baschetti, M.G., 2017b. Nanocellulose-based membranes for CO2 capture. J. Membr. Sci. 522, 216–225. https://doi.org/10.1016/J.MEMSCI.2016.09.024.

Auad, M.L., Contos, V.S., Nutt, S., Aranguren, M.I., Marcovich, N.E., 2008. Characterization of nanocellulose- reinforced shape memory polyurethanes. Polym. Int. 57, 651–659. https://doi.org/10.1002/pi.2394.

Baker, R.W., Low, B.T., 2014. Gas separation membrane materials: a perspective. Macromolecules 47, 6999–7013. https://doi.org/10.1021/ma501488s.

Balberg, I., Binenbaum, J., 1983. Computer study of the percolation threshold in a two-dimensional anisotropic system of conducting sticks. Phys. Rev. B 28, 3799–3812. https://doi.org/10.1103/PhysRevB.28.3799.

Brunetti, A., Scura, F., Barbieri, G., Drioli, E., 2010. Membrane technologies for CO2 separation. J. Membr. Sci. 359, 115–125. https://doi.org/10.1016/j.memsci.2009.11.040.

Chinga, G., Solheim, O., Morseburg, K., 2007. Cross-sectional dimensions of fiber and pore networks based on Euclidean distance maps. Nord. Pulp Pap. Res. J. 22, 500–507. https://doi.org/10.3183/NPPRJ-2007-22-04-p500-507.

Cuéllar-Franca, R.M., Azapagic, A., 2015. Carbon capture, storage and utilisation technologies: a critical analysis and comparison of their life cycle environmental impacts. J. CO2 Util. 9, 82–102. https://doi.org/10.1016/j.jcou.2014.12.001.

Dagnon, K.L., Shanmuganathan, K., Weder, C., Rowan, S.J., 2012. Water-triggered Modulus changes of cellulose nanofiber nanocomposites with hydrophobic polymer matrices. Macromolecules 45, 4707–4715. https://doi.org/10.1021/ma300463y.

Davis, S.J., Caldeira, K., Matthews, H.D., 2010. Future CO2 emissions and climate change from existing energy infrastructure. Science 80 (329), 1330–1333. https://doi.org/10.1126/science.1188566.

Deng, L., 2009. Development of Novel PVAm/PVA Blend FSC Membrane for CO2 Capture.

Deng, L., Hägg, M.-B., 2010. Swelling behavior and gas permeation performance of PVAm/PVA blend FSC membrane. J. Membr. Sci. 363, 295–301. https://doi.org/10.1016/J.MEMSCI.2010.07.043.

Deng, L., Kim, T.-J., Hägg, M.-B., 2009. Facilitated transport of CO2 in novel PVAm/PVA blend membrane. J. Memb. Sci. 340, 154–163. https://doi.org/10.1016/j.memsci.2009.05.019.

Dufresne, A., 2012. Nanocellulose: From Nature to High Performance Tailored Materials. De Gruyter, Berlin, Germany.

Ehmann, H.M.A., Mohan, T., Koshanskaya, M., Scheicher, S., Breitwieser, D., Ribitsch, V., Stana-Kleinschek, K., Spirk, S., 2014. Design of anticoagulant surfaces based on cellulose nanocrystals. Chem. Commun. 50, 13070–13072. https://doi.org/10.1039/C4CC05254D.

Favier, V., Dendievel, R., Canova, G., Cavaille, J.Y., Gilormini, P., 1997. Simulation and modeling of three-dimensional percolating structures: case of a latex matrix reinforced by a network of cellulose fibers. Acta Mater. 45, 1557–1565. https://doi.org/10.1016/S1359-6454(96)00264-9.

Favre, E., 2007. Carbon dioxide recovery from post-combustion processes: can gas permeation membranes compete with absorption? J. Membr. Sci. 294, 50–59. https://doi.org/10.1016/J.MEMSCI.2007.02.007.

Fujisawa, S., Okita, Y., Fukuzumi, H., Saito, T., Isogai, A., 2011. Preparation and characterization of TEMPO-oxidized cellulose nanofibril films with free carboxyl groups. Carbohydr. Polym. 84, 579–583. https://doi.org/10.1016/j.carbpol.2010.12.029.

Gamelas, J.A.F., Pedrosa, J., Lourenço, A.F., Mutjé, P., González, I., Chinga-Carrasco, G., Singh, G., Ferreira, P.J.T., 2015. On the morphology of cellulose nanofibrils obtained by TEMPO-mediated oxidation and mechanical treatment. Micron 72, 28–33. https://doi.org/10.1016/j.micron.2015.02.003.

Ghanadpour, M., Carosio, F., Larsson, P.T., Wågberg, L., 2015. Phosphorylated cellulose nanofibrils: a renewable nanomaterial for the preparation of intrinsically flame-retardant materials. Biomacromolecules 16, 3399–3410. https://doi.org/10.1021/acs.biomac.5b01117.

Ishii, D., Saito, T., Isogai, A., 2011. Viscoelastic evaluation of average length of cellulose nanofibers prepared by tempo-mediated oxidation. Biomacromolecules 12, 548–550. https://doi.org/10.1021/bm1013876.

Isogai, A., Saito, T., Fukuzumi, H., 2011. TEMPO-oxidized cellulose nanofibers. Nanoscale 3, 71–85. https://doi.org/10.1039/c0nr00583e.

Mulder, J., 1996. In: Mulder, J. (Ed.), Basic Principles of Membrane Technology, 2nd ed. Springer, Netherlands.

Jahan, Z., Niazi, M.B.K., Hägg, M.-B., Gregersen, Ø.W., 2018. Cellulose nanocrystal/PVA nanocomposite membranes for CO2/CH4 separation at high pressure. J. Membr. Sci. 554, 275–281. https://doi.org/10.1016/J.MEMSCI.2018.02.061.

Jalal Uddin, A., Araki, J., Gotoh, Y., 2011. Toward "strong" green nanocomposites: polyvinyl alcohol reinforced with extremely oriented cellulose whiskers. Biomacromolecules 12, 617–624. https://doi.org/10.1021/bm101280f.

Kim, T.-J., Li, B., Hägg, M.-B., 2004. Novel fixed-site-carrier polyvinylamine membrane for carbon dioxide capture. J. Polym. Sci. Part B: Polym. Phys. 42, 4326–4336. https://doi.org/10.1002/polb.20282.

Klug, H.P., Harold, P., Alexander, L.E., Leroy, E., 1974. X-Ray Diffraction Procedures for Polycrystalline and Amorphous Materials. John Wiley & Sons, NJ, USA.

Kumar, V., Ottesen, V., Syverud, K., Weiby Gregersen, Ø., Toivakka, M., 2017. Coatability of cellulose nanofibril suspensions: role of rheology and water retention. Bioresources 12, 7656–7679.

Li, W., Wu, Q., Zhao, X., Huang, Z., Cao, J., Li, J., Liu, S., 2014. Enhanced thermal and mechanical properties of PVA composites formed with filamentous nanocellulose fibrils. Carbohydr. Polym. 113, 403–410. https://doi.org/10.1016/j.carbpol.2014.07.031.

Liang, J., Huang, Y., Zhang, L., Wang, Y., Ma, Y., Cuo, T., Chen, Y., 2009. Molecular-level dispersion of graphene into poly(vinyl alcohol) and effective reinforcement of their nanocomposites. Adv. Funct. Mater. 19, 2297–2302. https://doi.org/10.1002/adfm.200801776.

Mahajan, R., Vu, D.Q., Koros, W.J., 2002. Mixed matrix membrane materials: an answer to the challenges faced by membrane based gas separations today? J. Chin. Inst. Chem. Eng. 33, 77–86.

McElroy, W.D., Glass, B., 1951. Phosphorus Metabolism 1 Johns Hopkins Press, MA, USA.

Mihranyan, A., Llagostera, A.P., Karmhag, R., Strømme, M., Ek, R., 2004. Moisture sorption by cellulose powders of varying crystallinity. Int. J. Pharm. 269, 433–442. https://doi.org/10.1016/j.ijpharm.2003.09.030.

Ottesen, V., Kumar, V., Toivakka, M., Chinga-Carrasco, G., Syverud, K., Weiby Gregersen, Ø., 2017. Viability and properties of roll-to-roll coating of cellulose nanofibrils on recycled paperboard. Nord. Pulp Pap. Res. J. 32, 179–188. https://doi.org/10.3183/NPPRJ-2017-32-02-p179-188.

Peppas, N.A., Merrill, E.W., 1976. Differential scanning calorimetry of crystallized PVA hydrogels. J. Appl. Polym. Sci. 20, 1457–1465. https://doi.org/10.1002/app.1976.070200604.

Postek, M.T., Moon, R.J., Rudie, A.W., Bilodeau, M.A., 2013. Production and Applications of Cellulose Nanomaterials. TAPPI, USA, pp. 21–25.

Rashad, A., Mustafa, K., Heggset, E.B., Syverud, K., 2017. Cytocompatibility of wood-derived cellulose nanofibril hydrogels with different surface chemistry. Biomacromolecules 18, 1238–1248. https://doi.org/10.1021/acs.biomac.6b01911.

Rescignano, N., Fortunati, E., Montesano, S., Emiliani, C., Kenny, J.M., Martino, S., Armentano, I., 2014. PVA bio-nanocomposites: a new take-off using cellulose nanocrystals and PLGA nanoparticles. Carbohydr. Polym. 99, 47–58. https://doi.org/10.1016/J.CARBPOL.2013.08.061.

Ricciardi, R., Auriemma, F., De Rosa, C., Lauprêtre, F., 2004. X-ray diffraction analysis of poly(vinyl alcohol) hydrogels, obtained by freezing and thawing techniques.

Macromolecules 37, 1921–1927. https://doi.org/10.1021/ma035663q.

Robeson, L.M., 2008. The upper bound revisited. J. Membr. Sci. 320, 390–400. https://doi.org/10.1016/j.memsci.2008.04.030.

Robeson, L.M., 1991. Correlation of separation factor versus permeability for polymeric membranes. J. Membr. Sci. 62, 165–185. https://doi.org/10.1016/0376-7388(91)80060-J.

Rodionova, G., Saito, T., Lenes, M., Eriksen, Ø., Gregersen, Ø., Kuramae, R., Isogai, A., 2013. TEMPO-mediated oxidation of Norway Spruce and Eucalyptus pulps: preparation and characterization of nanofibers and nanofiber dispersions. J. Polym. Environ. 21, 207–214. https://doi.org/10.1007/s10924-012-0483-9.

Sacui, I.A., Nieuwendaal, R.C., Burnett, D.J., Stranick, S.J., Jorfi, M., Weder, C., Foster, E.J., Olsson, R.T., Gilman, J.W., 2014. Comparison of the properties of cellulose nanocrystals and cellulose nanofibrils isolated from bacteria, tunicate, and wood processed using acid, enzymatic, mechanical, and oxidative methods. ACS Appl. Mater. Interfaces 6, 6127–6138. https://doi.org/10.1021/am500359f.

Saeed, M., Deng, L., 2016. Carbon nanotube enhanced PVA-mimic enzyme membrane for post-combustion CO_2 capture. Int. J. Greenh. Gas Control 53, 254–262. https://doi.org/10.1016/J.IJGGC.2016.08.017.

Saeed, M., Deng, L., 2015. CO_2 facilitated transport membrane promoted by mimic enzyme. J. Memb. Sci. 494, 196–204. https://doi.org/10.1016/J.MEMSCI.2015.07.028.

Saito, T., Isogai, A., 2004. TEMPO-mediated oxidation of native cellulose. The effect of oxidation conditions on chemical and crystal structures of the water-insoluble fractions. Biomacromolecules 5, 1983–1989. https://doi.org/10.1021/bm0497769.

Sandru, M., Kim, T.-J., Capala, W., Huijbers, M., Hägg, M.-B., 2013. Pilot scale testing of polymeric membranes for CO_2 capture from coal fired power plants. Energy Procedia 37, 6473–6480. https://doi.org/10.1016/j.egypro.2013.06.577.

Science, W., Vol, T., Dieti, C.B., 1970. The ultrastructure of cellulose from wood. Wood Sci. Technol. 4, 15–35. https://doi.org/10.1007/BF00367212.

Segal, L., Creely, J.J., Martin, A.E., Conrad, C.M., 1959. An empirical method for estimating the degree of crystallinity of native cellulose using the X-Ray diffractometer. Text. Res. J. 29, 786–794. https://doi.org/10.1177/004051755902901003.

Sharma, S.K., Prakash, J., Bahadur, J., Sudarshan, K., Maheshwari, P., Mazumder, S., Pujari, P.K., 2014. Investigation of nanolevel molecular packing and its role in thermo-mechanical properties of PVA–fMWCNT composites: positron annihilation and small angle X-ray scattering studies. Phys. Chem. Chem. Phys. 16, 1399–1408.

https://doi.org/10.1039/C3CP54054E.

Sharma, S.K., Prakash, J., Pujari, P.K., 2015a. Effects of the molecular level dispersion of graphene oxide on the free volume characteristics of poly(vinyl alcohol) and its impact on the thermal and mechanical properties of their nanocomposites. Phys. Chem. Chem. Phys. 17, 29201–29209. https://doi.org/10.1039/C5CP05278E.

Sharma, S.K., Prakash, J., Sudarshan, K., Sen, D., Mazumder, S., Pujari, P.K., 2015b. Structure at interphase of poly(vinyl alcohol)-SiC nanofiber composite and its impact on mechanical properties: positron annihilation and small-angle X-ray scattering studies. Macromolecules 48, 5706–5713. https://doi.org/10.1021/acs.macromol.5b01095.

Stuart Haszeldine, R., 2009. Carbon capture and storage: how green can black be? Science 80 (325), 1647–1652. https://doi.org/10.1126/science.1172246.

Sugiyama, J., Vuong, R., Chanzy, H., 1991. Electron diffraction study on the two crystalline phases occurring in native cellulose from an algal cell wall. Macromolecules 19924, 4168–4175.

Svagan, A.J., Hedenqvist, M.S., Berglund, L., 2009. Reduced water vapour sorption in cellulose nanocomposites with starch matrix. Compos. Sci. Technol. 69, 500–506. https://doi.org/10.1016/j.compscitech.2008.11.016.

Torstensen, J., Liu, M., Jin, S.A., Deng, L., Hawari, A.I., Syverud, K., Spontak, R.J., Gregersen, Y.W., 2018. Swelling and free-volume characteristics of TEMPO-Oxidized cellulose nanofibril films. Biomacromolecules 19, 1016–1025. https://doi.org/10.1021/acs.biomac.7b01814.

van Wazer, J.R., 1958. Phosphorus and Its Compounds, Interscience. Interscience Publishers, Inc.

Yu, D., Matteucci, S., Stangland, E., Calverley, E., Wegener, H., Anaya, D., 2013. Quantum chemistry calculation and experimental study of CO_2/CH_4 and functional group interactions for the design of solubility selective membrane materials. J. Membr. Sci. 441, 137–147. https://doi.org/10.1016/j.memsci.2013.03.052.

Zhou, Y.M., Fu, S.Y., Zheng, L.M., Zhan, H.Y., 2012. Effect of nanocellulose isolation techniques on the formation of reinforced poly(vinyl alcohol) nanocomposite films. Express Polym. Lett. 6, 794–804. https://doi.org/10.3144/expresspolymlett.2012.85.

Zornoza, B., Téllez, C., Coronas, J., 2011. Mixed matrix membranes comprising glassy polymers and dispersed mesoporous silica spheres for gas separation. J. Membr. Sci. 368, 100–109. https://doi.org/10.1016/j.memsci.2010.11.027.